

We are IntechOpen, the world's leading publisher of Open Access books Built by scientists, for scientists

6,900

Open access books available

185,000

International authors and editors

200M

Downloads

Our authors are among the

154

Countries delivered to

TOP 1%

most cited scientists

12.2%

Contributors from top 500 universities



WEB OF SCIENCE™

Selection of our books indexed in the Book Citation Index
in Web of Science™ Core Collection (BKCI)

Interested in publishing with us?
Contact book.department@intechopen.com

Numbers displayed above are based on latest data collected.
For more information visit www.intechopen.com



Fiber-Optic Ring Resonator Interferometer

Ramón José Pérez Menéndez

Abstract

In this chapter, theoretical analysis and electro-optical characterization of a fiber optic passive ring resonator interferometer (FOPRRI) were realized. First, a theoretical description and analysis of all-pass and add-drop filter configurations were performed, hence obtaining their respective transfer function, taking into account, the physical properties of a standard single-mode optical fiber as resonator constitutive material. Second, computational numerical simulations of a typical FOPRRI were performed with different analysis methods: effective index method (EIM), coupled mode theory (CMT), finite element method (FEM) and finite difference time domain (FDTD). Third, a comparative analysis of the results obtained with these methods is realized, showing the most accurate and appropriate for filter electro-optical characterization as a consequence. Last, and as an ultimate step, taking as reference the previously obtained electro-optical characterization for both configurations, the main applications are derived.

Keywords: passive optical ring resonator interferometer, single-mode optical fiber, all-pass filter, add-drop filter, EIM (effective index method), CMT (coupled mode theory), FEM (finite element method), FDTD (finite difference time domain)

1. Introduction

Optical interferometry constitutes an important technique used in high number of measurement processes for multiple physical magnitudes and quantitative phenomenon [1]. Particularly, fiber-optic waveguides can act as very useful and efficient transmission medium for light guidance in many interferometric sensor devices. The issue of fiber-optic interferometric devices has received an extensive treatment in the literature [2, 3]. Also, the general theory of optical resonators was extensively treated by authors, for example, Yariv and Yeh [4]. However, quantitative analytic treatment of a fiber optic passive ring resonator interferometer (FOPRRI) can be rather found in singular applications, particularly, in gyroscopes. A clear proof of it is that one of the pioneering and singular descriptions of fiber-optic ring interferometer devices was in 1976 when Vali and Shorthill designed the first fiber-optic gyroscope model [5–7]. Later, many other authors studied in detail this first design and improved some of its electro-optical parameters [8, 9]. Considered from a broader point of view, the FOPRRI device has now evolved toward what we could call the integrated optical passive ring resonator interferometer (IOPRRI). In this case, the fiber-optic ring resonator is replaced by a ring-integrated optical waveguide, made of high refractive index material, such as lithium niobate,

indium phosphide, silicon nitride, or silicon on insulator (SOI) platform. This chapter focuses on the analysis and testing of fiber-optic ring resonator. Therefore, the integrated ring resonator study, its investigations and challenges are beyond the scope of it [10].

An all-fiber passive ring resonator interferometer is formed by a directional coupler and a fiber-optic loop, as shown in **Figure 1**. Two main geometrical configurations are possible to reach such an optical coupling: (a) direct-coupled fiber ring resonator or (b) cross-coupled fiber ring resonator, as it can be seen in figure. Superimposition of successive beams generated by re-coupling the first coupled beam into the fiber ring results in multi-beam optical interference in a similar way to a Fabry-Pérot interferometer. Resonance will occur when the increase of the phase of the beam around the ring equals $2\pi n - (\pi/2)$, $\pi/2$ being the phase shift due to cross-coupling and n a positive integer ($n = 1, 2, 3, \dots$), so that the light reentering the ring after a single circulation around it is in phase with the light entering the ring for the first time. Following L. F. Stokes et al. [12, 13], the transfer function of the system for the optimum amplitude resonance condition is given by:

$$\frac{I_T}{I_0} = (1 - \gamma) \left\{ 1 - \left[\frac{(1 - \kappa)^2}{1 + \kappa^2 + 2\kappa \sin(\beta L)} \right] \right\} \quad (1)$$

where γ is the insertion loss of the coupler, $\kappa = (1 - \gamma) \exp(-2\alpha L)$ is the optical resonance coupling coefficient, α is the fiber attenuation factor, L is the total length of the fiber ring and β is the propagation constant of the re-circulating mode. The transfer function is very similar to a Fabry-Pérot interferometer operating in back-reflection mode. A finesse F of more of 1000 has been demonstrated for very low excess loss coupler and low-loss fibers [11, 12]. At resonance, significant optical power is recirculating in the ring and nonlinear effects as stimulated Brillouin scattering (SBS) can be observed for input powers of less than 100 μW [13]. As it will be seen later, fiber-optic ring resonators have been used in a number of applications, including fiber ring lasers [8], sensors [14], fiber laser gyroscopes [15, 16], optical spectrum analyzers [17, 18] and optical delay lines [19], among others. One of the first and main sensing applications of fiber-optic ring resonator is as a gyroscope and the major attraction of this kind of resonator gyro is that the cavity length can be taken much shorter than the convectional gyro in the ratio of $2/F$. In order to detect the phase shift induced by rotation, a highly coherent laser light source is required. A dual frequency modulation scheme is used to control the laser frequency and tracking the resonance condition [8, 9]. The difference between

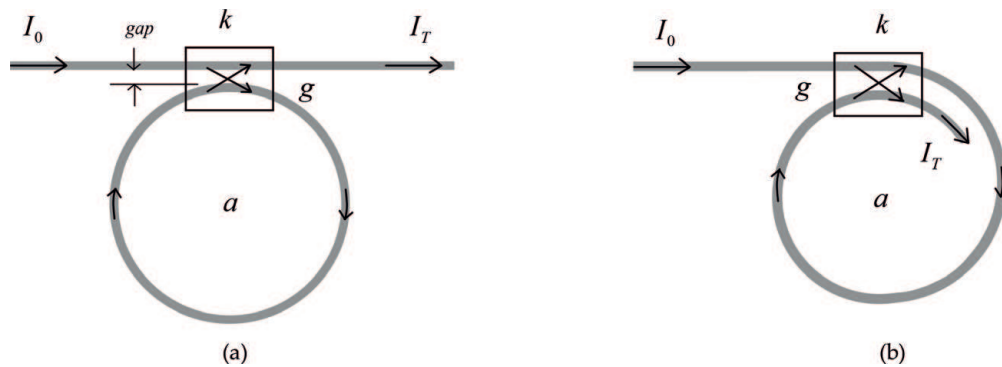


Figure 1. Fiber-optic-passive-ring-resonator-interferometer (FOPRRI) all-pass configuration: (a) direct-coupled fiber ring-resonator and (b) cross-coupled fiber ring-resonator.

these two frequencies gives a measure of gyro output signal, which, in turn, is proportional to rotation rate to which the fiber-optic ring resonator system is subjected.

2. Analysis of the fiber-optic all-pass filter ring resonator configuration

The all-pass ring resonator configuration is created by taking one output of a generic 2×2 directional coupler and feedback into one input, as it can be seen in **Figure 2**. Such a device exhibits a periodic cavity resonance when light traversing the ring acquires a phase shift corresponding to an integer multiple of 2π radians. The resonator can mathematically be formulated from two components: a coupling strength (from coupling coefficient κ) and a feedback path (via transmission coefficient t), in contrast to the infinite sum derivations made for Fabry-Perot and Gires-Tournois interferometers. Therefore, following the text of Rabus [20], we will derive the basic spectral properties by assuming the steady-state operation and the matching fields. Although both methods are equally valid, the field-matching method has the advantage of simplicity. The basic relations among the incident E_{i1} , transmitted E_{t1} , and circulating E_{i2} , E_{t2} fields of a single resonator are derived by combining the relations for the coupler with that of the feedback path. In the frequency domain, the fields exiting the coupling region are related to the input fields via the following equations:

$$E_{t1} = t E_{i1} + i \kappa E_{i2} \tag{2}$$

$$E_{t2} = t E_{i2} - i \kappa E_{i1} \tag{3}$$

where factor i is the imaginary unit ($i = \sqrt{-1}$) that takes into account, the phase shift caused by the cross-coupling of the waveguides. For simplicity, we assume the total symmetry of cross-coupling and bar-coupling coefficients for both waveguides, and therefore, the two approximate equations are ($\kappa_1 \approx \kappa_2 = \kappa$ and $t_1 \approx t_2 = t$). The two Eqs. (2) and (3) can be written in a compact way via the following unitary matrix:

$$\begin{pmatrix} E_{t1} \\ E_{t2} \end{pmatrix} = \begin{pmatrix} t & i \kappa \\ -i \kappa & t \end{pmatrix} \begin{pmatrix} E_{i1} \\ E_{i2} \end{pmatrix} \tag{4}$$

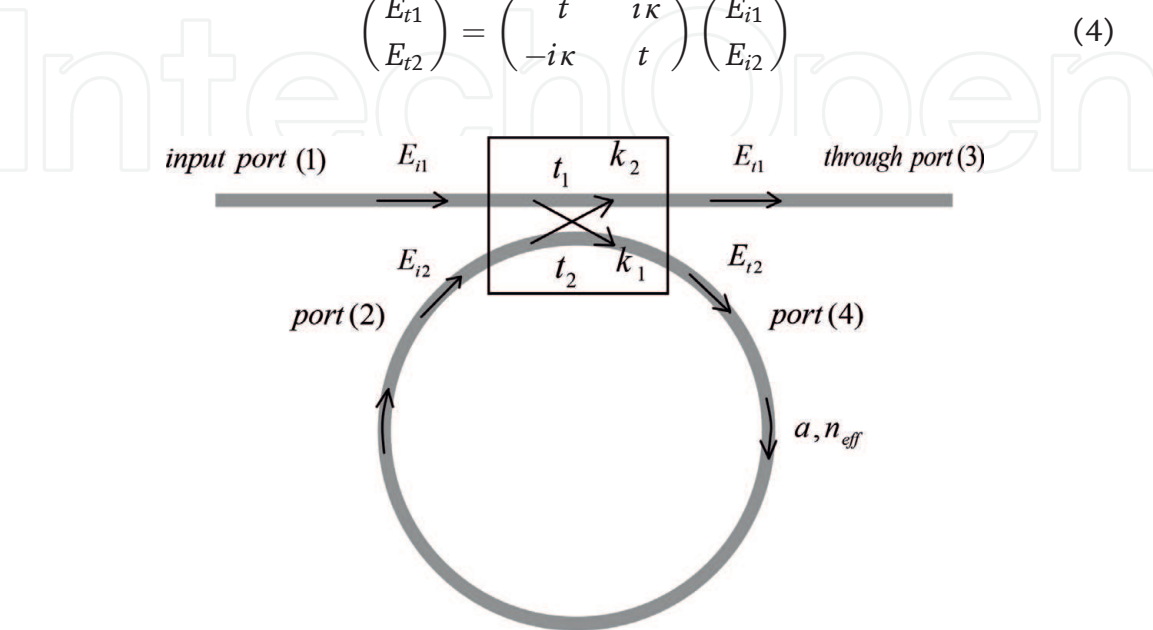


Figure 2.
All-pass fiber-optic ring resonator configuration ($\kappa_1 \approx \kappa_2 = \kappa$ and $t_1 \approx t_2 = t$).

where sign and i -factor in $i\kappa$ elements of first matrix on the right side of equation are due to cross-coupling phase shift caused by coupler. Also, since this matrix is an unitary matrix, we find that accomplishes the following relationship between bar- (t) and cross- (κ) coupling coefficients (assuming both are independent of frequency):

$$t^2 + \kappa^2 = 1 \quad (5)$$

The feedback path of length $2\pi R$ (R being the ring radius) connects the output from port 4 back into input port 2, where the field can be expressed as:

$$E_{i2} = e^{-\alpha 2\pi R} e^{i\beta 2\pi R} E_{t2} \equiv a e^{i\phi} E_{t2} \quad (6)$$

where α is the attenuation factor of the fiber, a -factor represents the ring single-pass field amplitude transmission (taking into account the fiber attenuation), $\beta = (2\pi/\lambda)n_{eff}$ is the propagation constant of propagating mode in the fiber (where in time, n_{eff} is the effective index of the fiber) and ϕ represents the single-pass ring round-trip phase shift.

Since that adding or subtracting an integer number m of 2π radians from single-pass phase shift does not change the value of the function, the single-pass phase shift for all resonances is defined such that its value is zero for a local resonance of interest. Furthermore, because the single-pass phase shift is directly related to the radian frequency as $\phi = \omega T_R$, where T_R is the transit time of the round-trip of ring resonator and then ϕ is clearly representative of a *normalized frequency detuning*. Following the previous derivations, one can demonstrate that the transmission power P_{t1} in the output port (3) of the straight waveguide can be expressed as:

$$P_{t1} = |E_{t1}|^2 = \frac{a^2 + |t|^2 - 2a|t| \cos(\phi + \phi_c)}{1 + a^2|t|^2 - 2a|t| \cos(\phi + \phi_c)} \quad (7)$$

where $t = |t| \exp(j\phi_c)$, $|t|$ representing the coupling losses and ϕ_c represents the phase of the coupler. Making a similar deduction, we can reach the circulating power in the ring, which is:

$$P_{i2} = |E_{i2}|^2 = \frac{a^2(1 - |t|^2)}{1 + a^2|t|^2 - 2a|t| \cos(\phi + \phi_c)} \quad (8)$$

On resonance, condition $(\phi + \phi_c) = 2\pi m$ is fulfilled, where m is an integer, and then Eqs. (7) and (8) becomes:

$$P_{t1} = |E_{t1}|^2 = \frac{(a - |t|)^2}{(1 - a|t|)^2} \quad (9)$$

$$P_{i2} = |E_{i2}|^2 = \frac{a^2(1 - |t|^2)}{(1 - a|t|)^2} \quad (10)$$

where, as we have said above, a is the loss coefficient of the ring (for zero loss $\alpha = 0$, then $a = 1$). The special case that occurs when $a = |t|$ (or $\kappa^2 = \alpha L$) is named *critical coupling* and is of high interest in applications. This happens when internal losses around the ring are equal to the coupling losses.

Then, the transmitted power to through port (3) becomes 0. The critical coupling is due to destructive interference between the direct beam and the cross-coupled beam of light, both after passing their respective coupling zone. A condition termed *undercoupling* does occur when the ring loss exceeds the coupling strength ($t > a$ or equally: $t^2 > \alpha L$, also $\kappa^2 < \alpha L$). An *overcoupling* condition takes place, when the round-trip loss does not exceed the coupling strength ($t < a$ or equally: $t^2 < \alpha L$, also $\kappa^2 > \alpha L$) and is the conventional mode of operation for an all-pass resonator. **Figure 3(a)** and **(b)** displays the effect of attenuation on the transmission and build-up factor for the overcoupled, critically coupled and undercoupled regimes. Experimental demonstration of the transmission characteristics in each of these regimes for a fiber all-pass filter ring resonator can be found in [22].

A good idea of the behavior of the system, when resonance condition accomplishes, can be obtained when one represents the *T transmission function* defined as the ratio P_{t1}/P_{i1} (i.e., the relationship between the through-port power and input-port power) versus normalized detuning ϕ , **Figure 3(a)**. Starting from input field expressions and after some derivations, the following equation can be found:

$$\mathcal{T} = \frac{P_{t1}}{P_{i1}} = \frac{|E_{t1}|^2}{|E_{i1}|^2} = \frac{a^2 - 2|t|a \cos \phi + |t|^2}{1 - 2|t|a \cos \phi + |t|^2 a^2} \quad (11)$$

Figure 3(a) represents the *T transmission function* for an all-pass ring resonator with $t = 0.75$ and varying loss a as a parameter (from $a = 0.00$ up to $a = 0.99$). It can be seen that, in this case, critical coupling occurs when $a = t = 0.75$; therefore, the *T transmission function* drops to zero when $\phi = 0$ for this a -factor value. As a

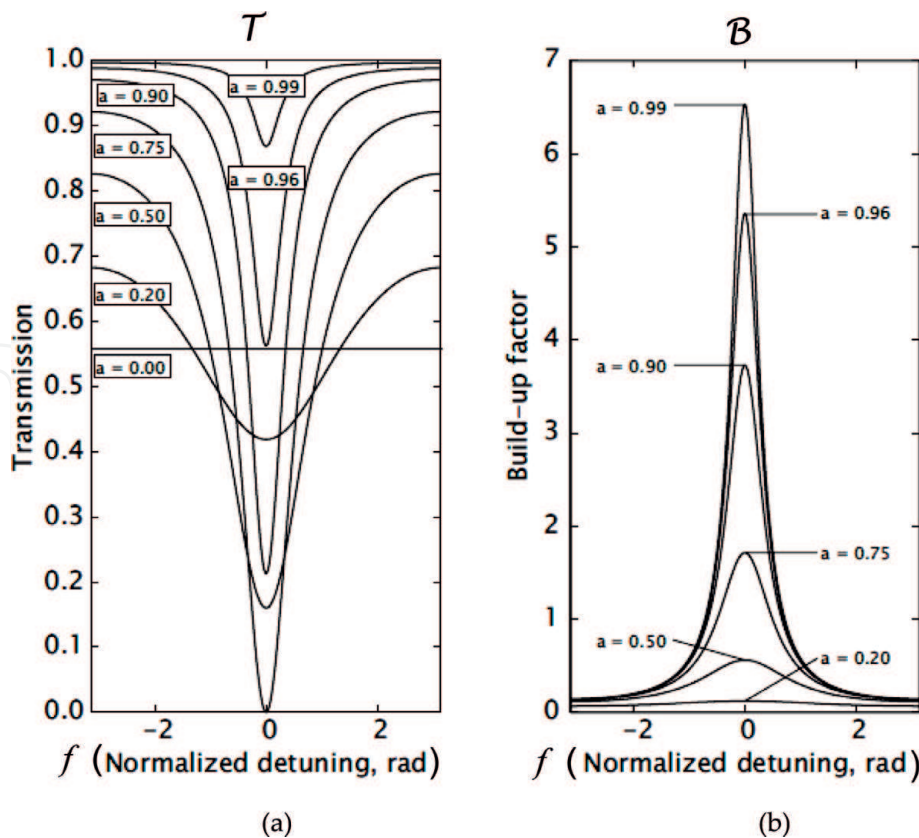


Figure 3. *T* transmission function (a) and *B* build-up factor (b) of ring-resonator, both as a function of normalized detuning ϕ , (curves extracted from [21], with permission).

increases (up to 1) or decreases (to 0.00) from 0.75, the corresponding transmission curve arises its minimum point from 0. For $a = 0.00$, T transmission function reaches a constant value of $0.75^2 = 0.5625$ for all values of ϕ . Another function that allows to obtain a good idea of the behavior of the system is the so-called *B intensity build-up factor* as a function of ϕ (normalized detuning), defined as:

$$B = \frac{P_{i2}}{P_{i1}} = \left| \frac{E_{i2}}{E_{i1}} \right|^2 = \frac{(1 - |t|^2) a^2}{1 - 2|t|a \cos \phi + |t|^2 a^2} \Rightarrow \lim_{\phi=2\pi m, a=1} \quad (12)$$

$$\frac{(1 - |t|^2) a^2}{1 - 2|t|a \cos \phi + |t|^2 a^2} = \frac{1 + |t|}{1 - |t|} \approx \frac{4}{\kappa^2}$$

B function can be thought as the ratio of the circulating light intensity inside the ring to incident light intensity. **Figure 3(b)** represents the B function (or intensity build-up factor) versus normalized detuning ϕ for the same all-pass ring than the one in **Figure 3(a)**, when varying loss a is taken as a parameter (from $a = 0.20$ up to $a = 0.99$). The last result in Eq. (12) refers to case in which incident light is resonant with the ring ($\phi = 2m\pi$) and attenuation is negligible ($a = 1$). This happens when constructive interference is produced at the coupler port (4) between the coupled light entering the ring coming from waveguide and the recirculation light coming from input port (3). This way, the circulating intensity of light around the ring results reinforced. However, for this constructive interference to take place, a coherent source is essential at input port (1). A passive ring resonator under these conditions attains the maximum ratio of circulating power to incident power that can be achieved. **Figure 4** shows two successive resonances versus normalized detuning with peak values given by right side of Eq. (12).

The spectral characteristics of the all-pass fiber-ring resonator configuration (one waveguide, one resonator, as represented in **Figure 2**) as optical filter can better be viewed when spectral response of through port versus vacuum wavelength is represented. A notch type filter is obtained from observation of this resonance curve (**Figure 5**). For cross-coupling value of 10% ($\kappa^2 = 0.10$), the optical intensity in the ring can be 40 times higher than the intensity in the input port of the waveguide. This way, since the intensity in the fiber ring can be much higher

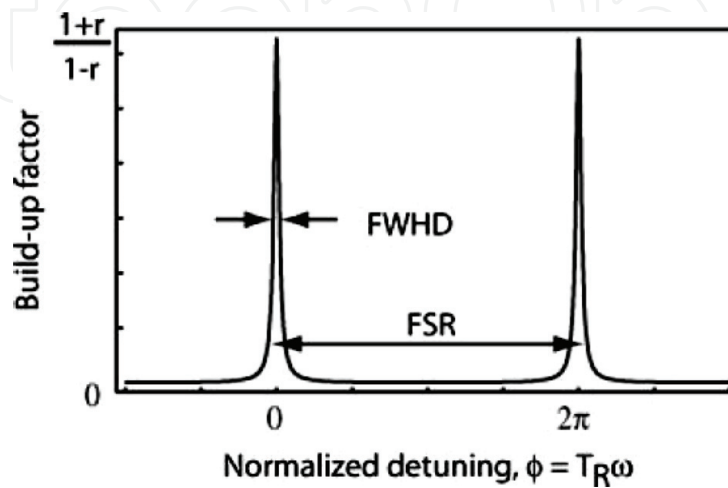


Figure 4.
Build-up factor versus normalized detuning for all-pass fiber ring resonator (from [21], with permission).

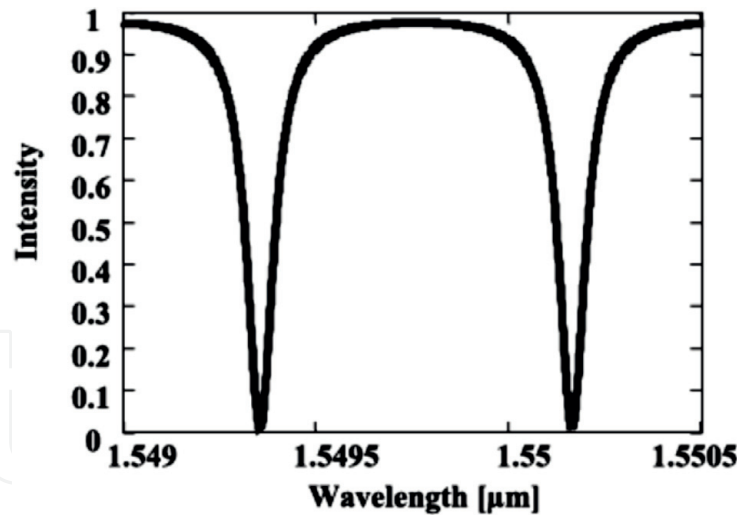


Figure 5.
 Spectral response of through port of an all-pass fiber ring resonator (notch-type filter).

than in the bus, fiber ring resonators can be used for nonlinear optics applications with low input intensities.

Ring resonator filters can be characterized by four parameters, which are generally used to describe their performance, namely, the *free spectral range* (FSR), the *full width at half maximum* (FWHM), the *finesse* F and the *quality factor* Q . The FSR $\Delta\lambda$ is the distance between two successive resonance peaks (difference between the wavelengths corresponding to two successive resonant conditions). When neglecting the wavelength dependence of the fiber-optic effective refractive index n_{eff} , approximate calculation of FSR $\Delta\lambda$ is very simple [20], as follows:

$$FSR = \Delta\lambda = -\frac{2\pi}{L} \left(\frac{\partial\beta}{\partial\lambda} \right)^{-1} \approx \frac{\lambda^2}{n_{eff}L} \quad (13)$$

This approximation is derived from the resonant condition next to a resonance found for the used propagation constant. A more accurate calculation is obtained taking into account the chromatic dispersion of the fiber. Then, the group refractive index of the fiber can be used instead of the effective index, so that the new expression for FRS to be:

$$FSR = \Delta\lambda = \frac{\lambda^2}{n_g L} \quad (14)$$

The second parameter in importance for describing the performance of the optical filter is the FWHM. It is defined as the full spectral width at half maximum (or 3 dB bandwidth $2\delta\lambda$). In the case of all-pass filter, FWHM must be redefined as full width at half depth (FWHD) and its value can be calculated as follows (in absence of ring internal losses, that is, $a = 1$):

$$FWHD = 2\delta\lambda = \frac{\lambda^2}{2\pi^2 n_g R} \frac{1 - |t|}{\sqrt{|t|}} \xrightarrow{|t| \approx 1} \approx \frac{\lambda^2 \kappa^2}{4\pi^2 n_g R} \quad (15)$$

Third parameter is the finesse F . The finesse is a figure of merit of the filter that can be defined as the ratio between FSR and FWHD. So that implementing this

definition and in absence of ring internal losses, the resulting expression for the finesse of an all-pass fiber resonator is [23]:

$$\mathcal{F} = \frac{FSR}{FWHD} \approx \frac{\frac{\lambda^2}{2\pi n_g R}}{\frac{\lambda^2 \kappa^2}{4\pi^2 n_g R}} = \frac{2\pi}{\kappa^2} \quad (16)$$

Finally, the fourth parameter is the quality factor Q . It represents a measure of the sharpness of the resonance. It can be defined as the ratio of the operation wavelength and the resonance width (FWHD). Its calculation is as follows:

$$Q = \frac{\lambda}{FWHD} \approx \frac{\lambda}{\frac{\lambda^2 \kappa^2}{4\pi^2 n_g R}} = \frac{\lambda}{\frac{\lambda^2 \kappa^2}{2\pi n_g L}} = \frac{2\pi n_g L}{\lambda \kappa^2} = \frac{n_g L}{\lambda} \mathcal{F} \quad (17)$$

The quality factor Q can also be regarded as the total energy stored in the ring divided by the energy lost per optical cycle.

3. Analysis of the fiber-optic add-drop filter ring resonator configuration

The basic fiber-optic add-drop filter consists of one input-waveguide, one output-waveguide and one fiber-ring resonator such as the one represented in **Figure 6**. Both of the waveguides are side-coupled to ring resonator. The four ports of structure are defined as input port, throughput port, drop port and add port. Viewed from drop port acting as the optical output, this configuration behaves as a narrow-band amplitude filter that can add or drop a spectral band from an optical input. This configuration is mathematically equivalent to a well-known Fabry-Pérot interferometer. Therefore, the equations for transmission coefficients are easy to obtain. For simplification, E_{i1} is defined with unitary rms amplitude. Then, the throughput E_{t1} mode rms amplitude in the input-waveguide is given by:

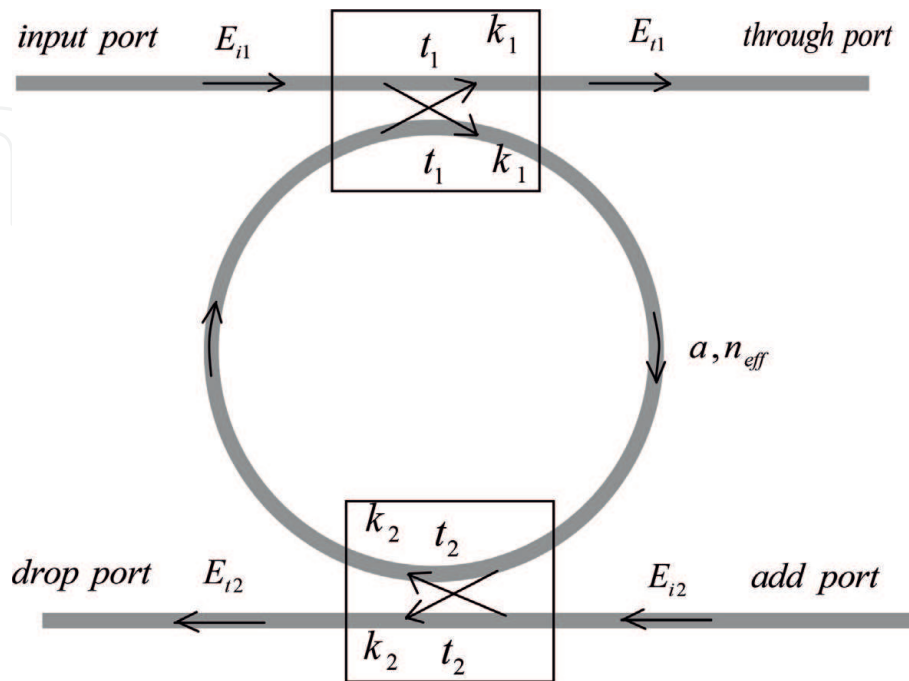


Figure 6. Add-drop fiber-optic ring resonator configuration (for symmetrical coupling: $\kappa_1 \approx \kappa_2 = \kappa$ and $t_1 \approx t_2 = t$).

$$E_{t1} = \left[t_1 + \frac{t_2 \kappa_1 \kappa_2 a_{1/2}^2 e^{j\theta(|t_1|^2 + |\kappa_1|^2)}}{1 - t_1 t_2 a_{1/2}^2 e^{j\theta}} \right] E_{i1} = \frac{t_1 - t_2 a e^{j\theta}}{1 - t_1 t_2 a e^{j\theta}} \quad (18)$$

In this equation, $a_{1/2}$ and $\theta_{1/2}$ are used, which are the half round-trip loss and phase, respectively. It is $a = a_{1/2}^2$ and $\theta = 2\theta_{1/2}$. The mode amplitude in the ring has to pass the second coupler to become the new dropped mode rms amplitude E_{t2} . Its rms amplitude value is given by:

$$E_{t2} = \frac{\kappa_1 \kappa_2 a_{1/2} e^{j\theta_{1/2}}}{1 - t_1 t_2 a e^{j\theta}} \quad (19)$$

At resonance condition ($\theta = m 2\pi$, m integer), the output intensity from the drop port is given by:

$$P_{t2-resonance} = |E_{t2-resonance}|^2 = \frac{(1 - t_1^2)(1 - t_2^2)a}{(1 - t_1 t_2 a)^2} \quad (20)$$

The through port mode amplitude E_{t1} will be zero at resonance for identical symmetrical couplers ($t_1 = t_2$), when $a = 1$ (zero loss). This means that on resonance, all input optical power will be coupled to resonator and could be extracted by drop port. The value $a = 1$ (zero loss) can only be achieved by a given value of gain incorporated in the resonator ring to compensate the waveguide losses. In a pure passive ring resonator with defined waveguide constituents, the loss coefficient a is constant. By adjusting coupling parameters t_1 and t_2 to the loss coefficient a , minimum intensity can be achieved (ideally, $P_{t1} \approx 0$). From Eq. (18), one can obtain:

$$a = \frac{t_1}{t_2} \quad (21)$$

According with Eq. (18), the transfer function of through port (relative to input port) is given by:

$$\mathcal{T}_{through} = \left| \frac{E_{t1}}{E_{i1}} \right|^2 = \frac{t_2^2 a^2 - 2 t_1 t_2 a \cos \phi + t_1^2}{1 - 2 t_1 t_2 a \cos \phi + (t_1 t_2 a)^2} \xrightarrow{a=1, t_1=t_2=t} \frac{\frac{4t^2}{(1-t^2)^2} \sin^2\left(\frac{\phi}{2}\right)}{1 + \frac{4t^2}{(1-t^2)^2} \sin^2\left(\frac{\phi}{2}\right)} \quad (22)$$

Taking into account, Eq. (19), the transfer function of drop port (relative to input port), will be:

$$\mathcal{T}_{drop} = \left| \frac{E_{t2}}{E_{i1}} \right|^2 = \frac{(1 - t_1^2)(1 - t_2^2)a}{1 - 2 t_1 t_2 a \cos \phi + (t_1 t_2 a)^2} \xrightarrow{a=1, t_1=t_2=t} \frac{1}{1 + \frac{4t^2}{(1-t^2)^2} \sin^2\left(\frac{\phi}{2}\right)} \quad (23)$$

This way, the transmission spectral response of through port corresponds to an approximately Lorentzian curve centered on a resonance, where a narrow frequency band has been extracted (see **Figure 7**). These extracted band do appear (in inverted shape) in the spectrum response of drop port, as it can also be seen in same figure. In the case of add-drop filter, if attenuation is negligible ($a \approx 1$), *critical coupling* occurs at symmetric coupling ($\kappa_1 = \kappa_2 = \kappa$). For non-negligible single-pass resonator loss, critical coupling occurs when single-pass ring losses match the

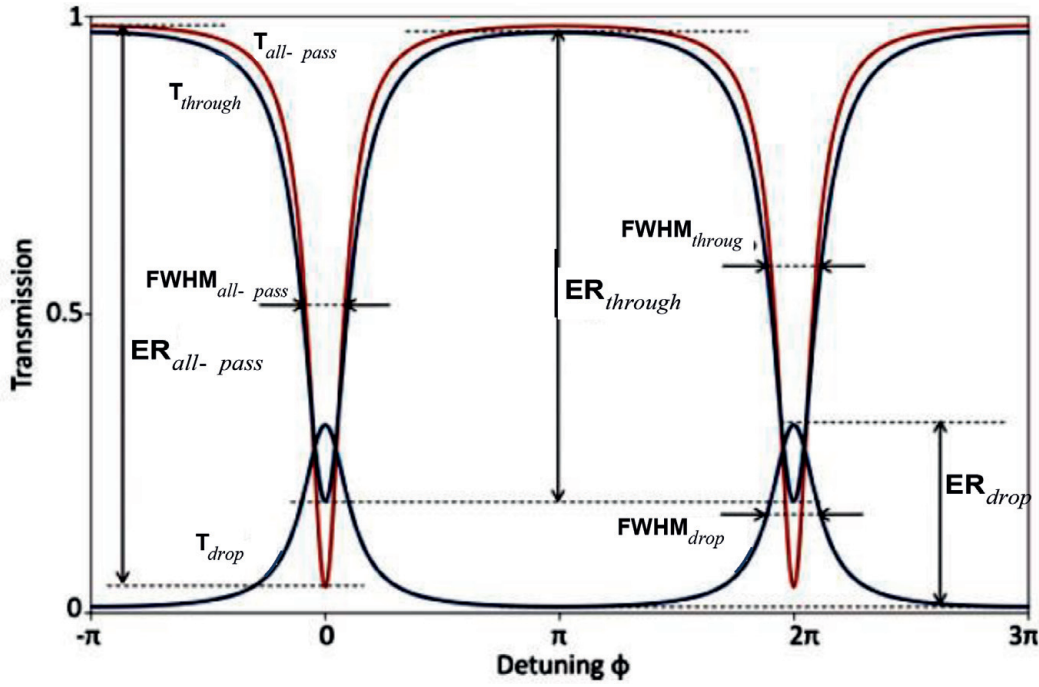


Figure 7.
Spectral response of a fiber-optic add-drop filter (adapted from [24], with permission).

coupling, so it verified the following condition: $t_2 a = t_1$. Transfer functions, FWHM and extinction ratio (ER) relative to all-pass filter, through and drop ports of add-drop filter are plotted.

It is worth to make an interpretation and comparison of the add-drop filter configuration with respect to the all-pass filter one. In the upper coupler (**Figure 6**), interference takes place between the coupled input field and ring circulating field. However, the lower coupler does not experience any interference (provided that excitation is from the upper waveguide only). The lower coupler may thus be viewed simply as a tap waveguide that leaks power out of the ring into the drop port. For an add-drop filter, it is desirable to operate at critical coupling for achieving the complete extinguishment of a frequency band in the through port. In this case, the sum of all losses incurred in the resonator, even the loss at the out-coupled drop port, must be taken into account. Calculations of FSR, FWHM, B build-up factor, finesse \mathcal{F} and quality factor Q are given below according to the results found in Refs. [21, 22].

$$FSR = \Delta\lambda = \frac{\lambda^2}{n_{eff} L} \quad (24)$$

$$FWHD \approx \frac{\lambda^2 \kappa^2}{\pi L n_{eff}} \quad (25)$$

$$\mathcal{F} = \frac{FSR}{FWHD} \approx \frac{\pi}{\kappa^2} \quad (26)$$

$$Q = \frac{\lambda}{FWHD} \approx \frac{\pi n_g L}{\lambda \kappa^2} = \frac{n_g L}{\lambda} \mathcal{F} \quad (27)$$

where the approximations again apply to symmetrically coupled, low-loss and weakly coupled microrings. Note that, comparing Eqs. (27) and (17), with the same optical parameters, add-drop filter has the half value of Q -factor (and also the finesse \mathcal{F}) than that the all-pass one. This result could be expected since an all-pass filter configuration has half the loss due to external coupling than an add-drop one.

4. Numerical simulation of fiber-optic all-pass filter ring resonator configuration

As announced at the beginning of this chapter, this section will deal specifically with the numerical simulation of a typical FOPRRI in all-pass filter configuration. First, effective index method (EIM) [25, 26] will be applied to this structure in which main constituents are made of a standard single-mode optical fiber (coupler and ring resonator). Secondly, coupled mode theory (CMT) [27–33] will be performed to the same structure. In third time, finite element method (FEM) [34] is performed. Finally, 3D-FDTD (finite difference time domain) [35, 36] was applied to same structure. The results of all these numerical simulations are compared to each other to see which one best match each specific application.

Optical layout scheme for EIM and CMT numerical simulation is represented in **Figure 8**. OptSim[®] Circuit tool (from Synopsys[™] Software) was applied to obtain the transmission power spectrum of this resonant structure, which takes the effective index method (EIM) as a numerical simulation algorithm. A side-polished fiber-optic 4×4 directional coupler is used to couple the waveguide fiber to fiber ring resonator (here implemented by a series of two waveguides, 1 and 2, respectively). A standard SMF-28 (Corning[™] Glass) single-mode optical fiber is assumed for both, waveguide and ring resonator as constituent materials. Optical parameters of this fiber are: basis material = fused-silica (core = boron-silicate, cladding = silica), step refractive index, core diameter = $8.2 \mu\text{m}$, cladding diameter = $125 \mu\text{m}$, effective refractive indexes: $n_{\text{core}} = 1.467$, $n_{\text{cladding}} = 1.460$, numerical aperture (NA) = 0.143, maximum attenuation = 0.35 dB/km (at 1310 nm wavelength) and h-parameter = $2 \times 10^{-6} \text{ m}^{-1}$. Gap between waveguide and ring resonator is 200 nm. Normalized Gaussian profile continuous wave (CW) optical field of 1310 nm vacuum wavelength was launched to the system from a wideband tunable laser source. To obtain the pass-through port power transmission spectrum, wavelength sweeping of laser source was made in order to fix each wavelength value for its respective measured optical power. The computation is iterated 30 times to obtain the steady-state solution. Obtained transmission power spectrum is represented in **Figure 9**.

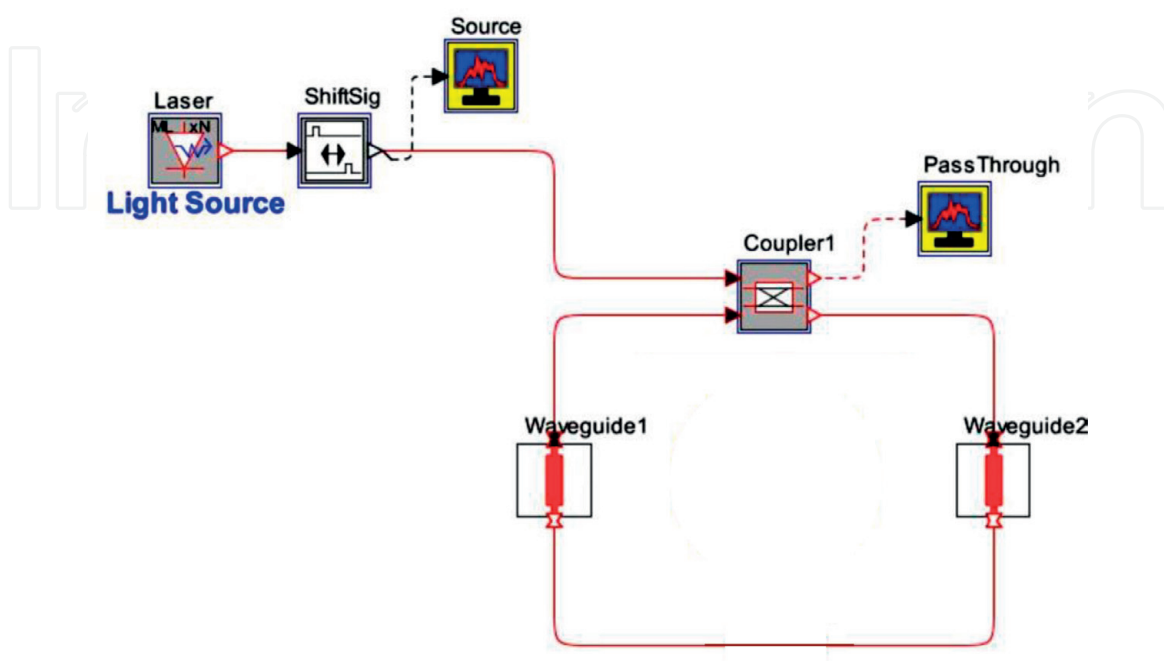


Figure 8.
 All-pass FOPRRI configuration: optical layout scheme for EIM and CMT numerical simulations.

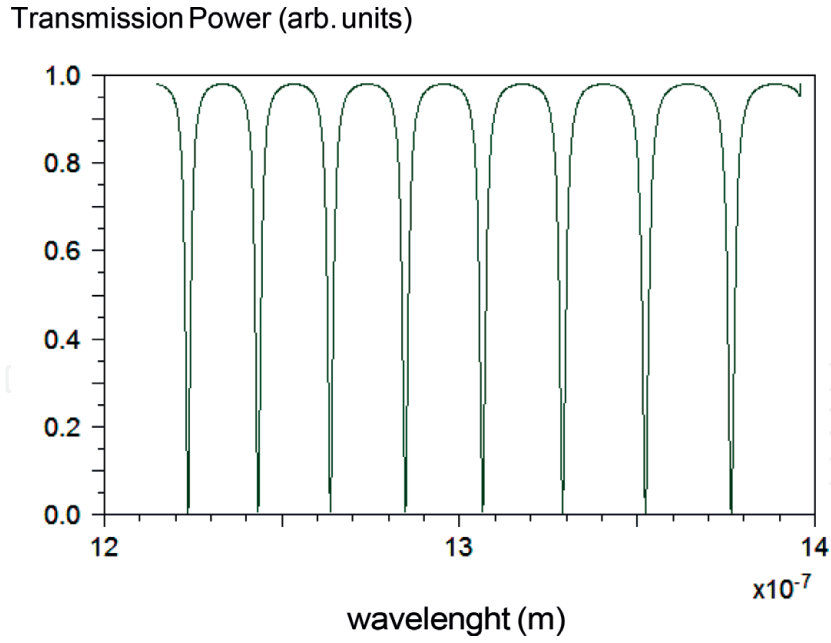


Figure 9.
All-pass FOPRRI configuration: transmission power spectrum.

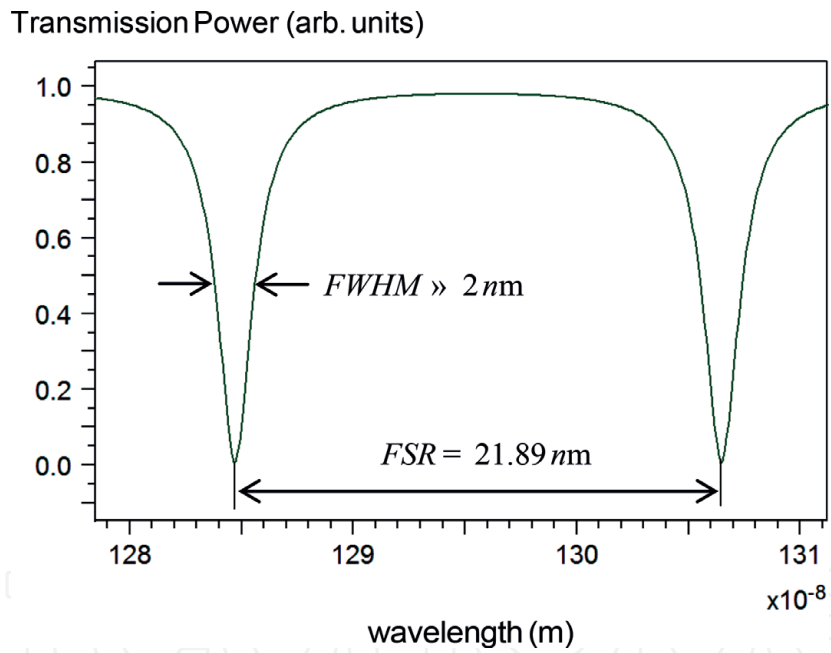


Figure 10.
All-pass FOPRRI configuration: expanded transmission power spectrum around 1295 nm.

As it can be seen on expanded transmission spectrum showed in **Figure 10**, a resonance condition is achieved for 1285 nm wavelength. Since the effective refractive index of ring resonator is 1.467 and its optical path length is 51.420 μm , a FSR of 21.89 nm is obtained as it can also be observed in this same figure. This value agrees accurately with theoretical value as calculated from Eq. (13).

On the other hand, measured value of FWHM is approximately 2 nm. This value is also in frank agreement with value calculated analytically by means of Eq. (15), taking into account 8.184 μm as medium ring resonator radius. Then, a calculation from Eq. (16) gives the value of 10.95 for F finesse. As a consequence of last, calculation from Eq. (17) yields 642.80 for the Q quality-factor of the system.

Coupled mode theory (CMT), which uses BPM method, was applied to this structure by means of BeamPROP[®] tool (Synopsys[™] Software) [32]. This method

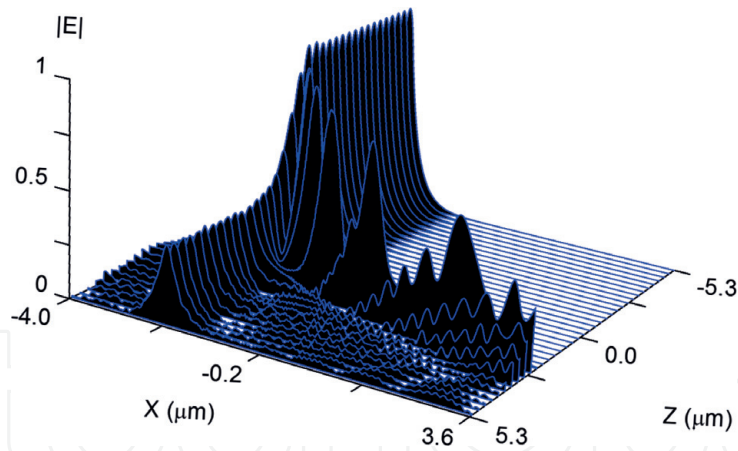


Figure 11.
 CMT method numerical simulation result (from BeamPROP[®] tool) for all-pass FOPRRI configuration (resonance at 1285 nm).

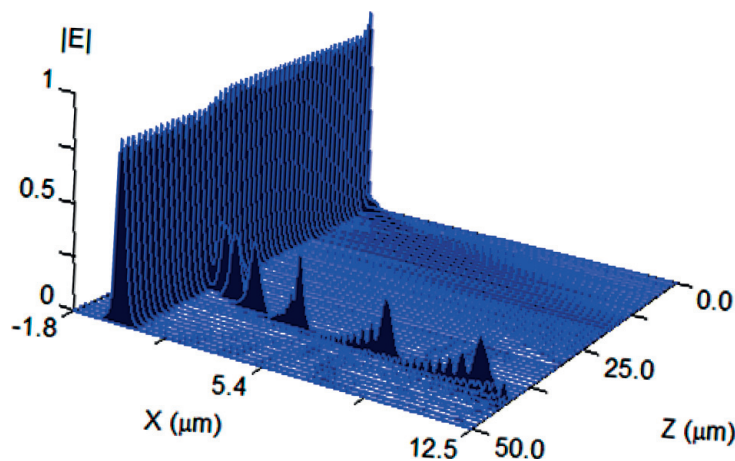


Figure 12.
 FEM numerical simulation (from FemSIM[®] tool) for all-pass FOPRRI configuration (resonance at 1285 nm).

also takes into account the effective index of the ring resonator material, so the expected results from it will be improved compared with those obtained with the EIM method alone. Further in-depth readings on BPM method can be found in Refs. [37–42]. **Figure 11** shows the result of numerical simulation of all-pass ring resonator considered here.

Finite element method (FEM) was applied to this structure by means of FemSIM[®] tool (Synopsys[™] Software) [34]. This method also takes into account the effective index of the ring resonator material, so the expected results from it will be improved compared with those obtained with the EIM method alone. Additional treatment on the FEM method can be found in the Refs. [43–47]. The result of FemSIM[®] of all-pass ring resonator analyzed here is represented in **Figure 12**.

FullWAVE[®] (Synopsys[™] Software) [36] is a full-vectorial numerical computation tool that allows the simulation of light wave propagation in an arbitrary geometry system. The simulation engine is based on the finite difference time domain (FDTD) method. The FDTD algorithm implements rigorous and complete time-space solution to Maxwell's equations. This method offers an efficient field wave propagation solution in a photonic-integrated structure when other methods such as beam propagation method (BPM) or finite element method (FEM) cannot cope with the structure geometry or do not provide a precise solution. Additional treatment on the FDTD method can be found in Refs. [48–52]. **Figure 13** represents the result of FDTD numerical simulation of all-pass ring resonator studied here.

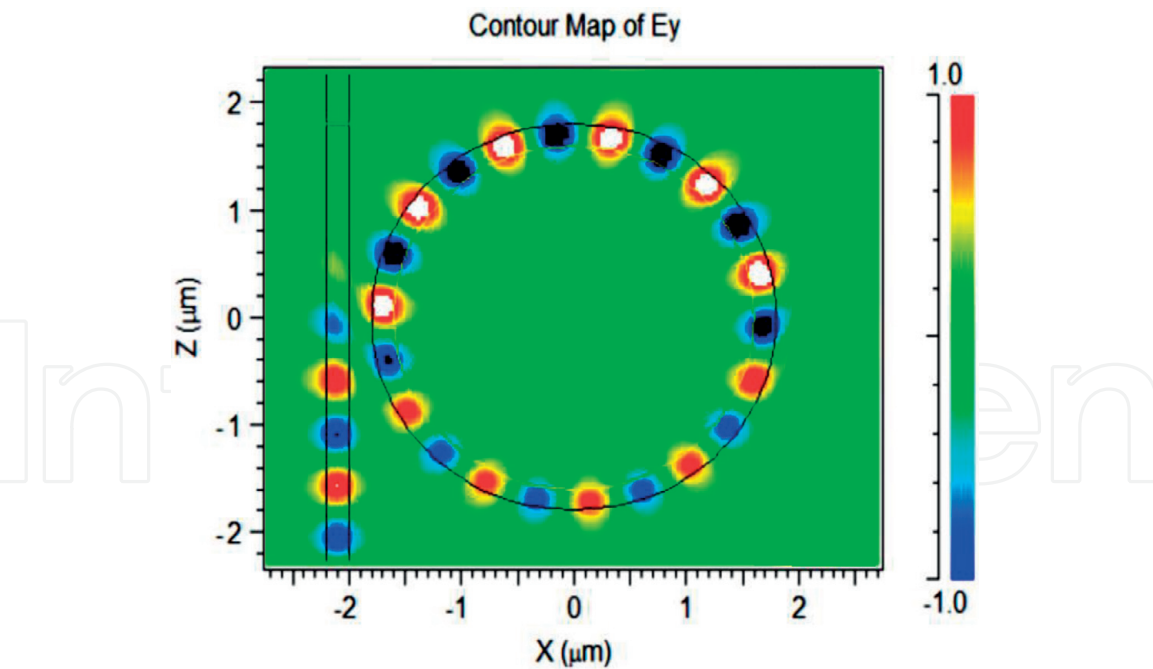


Figure 13.
2D-FDTD numerical simulation results for an all-pass FOPRRI (resonance at 1285 nm).

Comparison	EIM	CMT (BPM)	FEM	FDTD
All-pass filter	Good	Very good	Outstanding	Excellent
Add-drop filter	Good	Very good	Outstanding	Excellent

Table 1.
Comparison of numerical simulation methods (EIM, CMT, FEM and FDTD) for all-pass/add-drop filters.

Table 1 shows a comparison of the results of the four methods used (EIM, CMT, FEM and FDTD) for all-pass filter and add-drop filter configurations, taking into account their suitability for accuracy and calculation time. In view of transmission spectrum of the all-pass filter configuration, this can find applications such as optical band-pass filter, optical delay line, optical switch and active ring modulator.

5. Numerical simulation of fiber-optic add-drop filter ring resonator configuration

As realized on all-pass configuration, this section will be dedicated to numerical simulation of a typical FOPRRI in add-drop filter configuration. Then, successive numerical simulations by applying effective index method (EIM), coupled mode theory (CMT), finite element method (FEM) and 3D finite difference time domain (FDTD) will be performed to this configuration. Finally, the comparison of all these numerical simulations will be carried out to verify, which is the most appropriate for each type of application.

Optical layout scheme for EIM and CMT numerical simulation is represented in **Figure 14**. OptSim[®] Circuit tool (from Synopsys[™] Software) with the effective index method (EIM) as computational algorithm was applied here to obtain the transmission power spectrum of resonant structure. The configuration analyzed can be obtained from the one considered in Section 4 by adding a second fiber 4 × 4 directional coupler and a second side-coupled fiber waveguide. Also, standard SMF-28 (Corning[™] Glass) single-mode optical fiber is assumed for both, upper and

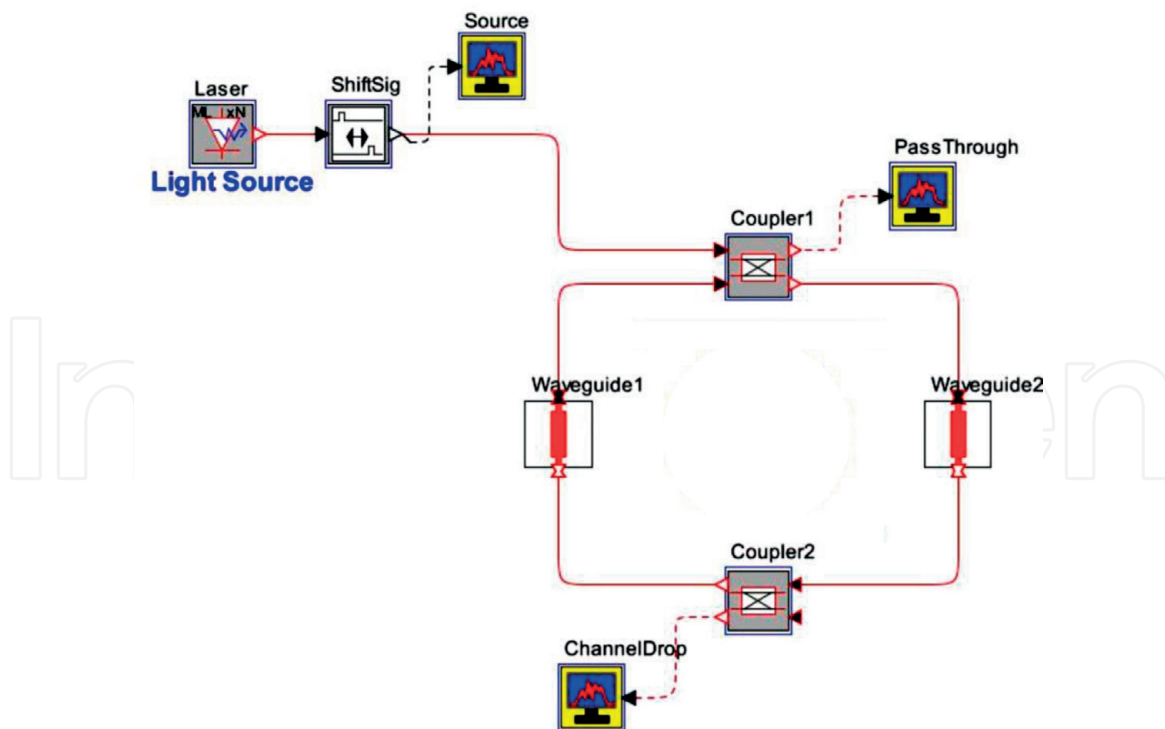


Figure 14.
 Add-drop FOPRRI configuration: optical layout scheme for EIM and CMT numerical simulations.

lower waveguides and ring resonator as constituent material. Gap between waveguide and ring resonator is 200 nm. Normalized Gaussian profile continuous wave (CW) optical field of 1310 nm vacuum wavelength was launched to the system from a wideband tunable laser source. To obtain the power transmission spectra of pass-through and drop ports, wavelength sweeping of laser source was made in order to fix each wavelength value for its respective measured optical power. The computation is iterated 30 times to obtain the steady-state solution. The resulting transmission power spectra are depicted in **Figure 15(a)–(c)**, respectively. As it can be seen on expanded drop-port transmission spectrum showed in **Figure 10(c)**, a resonance condition is achieved for 1285 nm wavelength. Since the effective refractive index of ring resonator is 1.467 and its optical path length is 51.420 μm , a FSR of 21.89 nm is obtained as it can also be observed in this same figure. This value agrees accurately with theoretical value as calculated from Eq. (24). On the other hand, measured value of FWHM is approximately 4 nm. This value is also in frank agreement with value calculated analytically by means of Eq. (25).

Then, a calculation from Eq. (26) gives the value of 5.475 for F finesse. As a consequence of last, calculation from Eq. (27) yields 321.40 for the Q quality-factor of the system. These results are the expected, taking into account that for the same coupling coefficients, waveguide and ring resonator geometry, the values F and Q for add-drop configuration must be half than those for the all-pass ones.

Comments about fundamentals and particularities of BPM, FEM and FDTD methods are given in the following. For an optical waveguide as cylindrical optical fiber, where light travels almost completely confined to its core medium, propagation mechanism can be simply described by means of the four Maxwell's equations. Then, BPM, FEM and FDTD methods assume that the solution to Maxwell's equations follows the slowly varying envelope approximation. This means that the field's amplitude variation is very small as compared to the variation in the phase and propagation distance. BPM is a fast method, which is applicable to a system whose physical structure and properties vary slowly with the geometry. The FDTD method uses the standard finite difference method to solve the Maxwell's equations. It is also

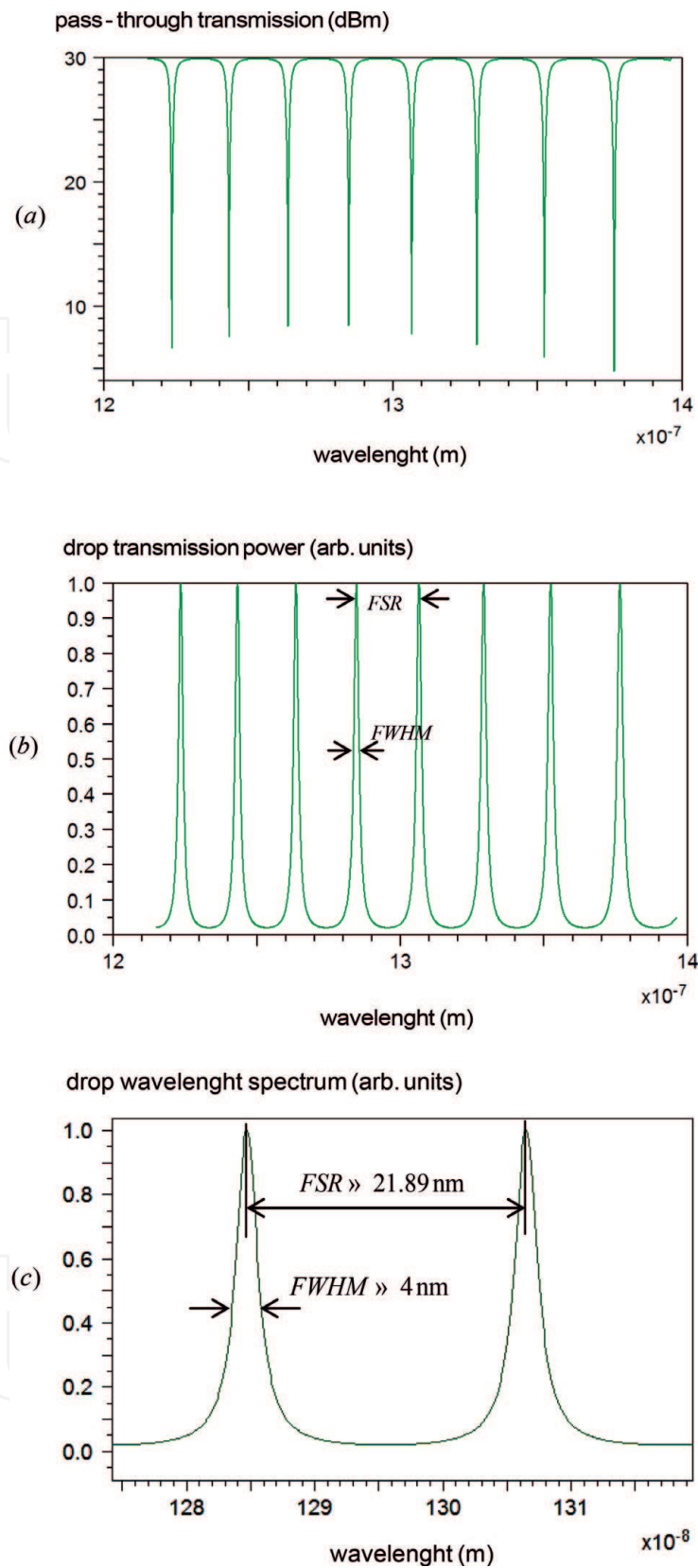


Figure 15. Transmission spectra of add-drop configuration: (a) pass-through port, (b) drop port and (c) drop-port (expanded).

known as the full wave method. It discretizes the equations and solves them using a linear algebraic algorithm.

To accelerate the finite difference method simulation, standard approaches such as Krylov subspace-based model order reduction or multi-grid analysis are used. It can be used for all types of structures. As compared with BPM, FDTD is at least an order of magnitude slower. The basic elements that are of application in the case of

FDTD method allow as broad as the Maxwell's equations they embody in discretized form, the basic formulation using centered finite difference expressions, which can treat virtually any material type and geometry and the basic resources needed to implement the technique. The FDTD method treats transients in the time domain (e.g., pulses), and it is applicable over the computationally unpredictable resonance region in which a wavelength is comparable with to the object interaction size. The FDTD method offers many advantages as an electromagnetic modeling, simulation and analysis tool. Its capabilities include: 1) broadband response predictions centered about the system resonances, 2) arbitrary 2-D or 3-D model geometries, 3) interaction with an object of any conductivity from that of a perfect conductor, to that of a real metal, to that of low or zero conductivity, 4) frequency-dependent constitutive parameters for modeling most materials (lossy dielectrics, magnetic materials, anisotropic plasmas and magnetized ferrites) and 5) any type of response, including far fields derived from near fields, such as scattered fields, antenna patterns, radar-cross sections, surface response, current and power density and penetration/coupling. FDTD is an appropriate technique for time-domain analysis of passive microwave and millimeter wave structures. The strength of FDTD method lies in its capability to model any volumetric structure with what are typically rectangular cells. No requirements for symmetry or smooth surfaces are needed. Also, FDTD has been successfully used in modeling micro-structured micro-strip structures.

Coupled mode theory (CMT), which uses BPM method, was applied to this structure by means of BeamPROP[®] tool (Synopsys[™] Software). This method also takes into account the effective index of the ring resonator material, so the expected results from it will be improved compared with those obtained with the EIM method alone. BPM numerical simulation results can be seen in **Figure 16**.

Finite element method (FEM) was applied to this structure by means of FemSIM[®] tool (Synopsys[™] Software). This method also takes into account the effective index of the ring resonator material, so the expected results from it will be improved compared with those obtained with the EIM method alone. FEM numerical simulation of this case is represented in **Figure 17**.

Result of a FDTD method numerical simulation applied to the add-drop filter configuration considered here is represented on **Figure 18** (resonance takes place at 1285 nm wavelength). As it was said above, for this structure Eq. (25) gives the value of 5.475 for F finesse and Eq. (26) yields 321.40 for the Q quality-factor of the system.

As a consequence of transmission spectrum of add-drop filter configuration, this can find applications such as optical band-pass filter, optical delay line,

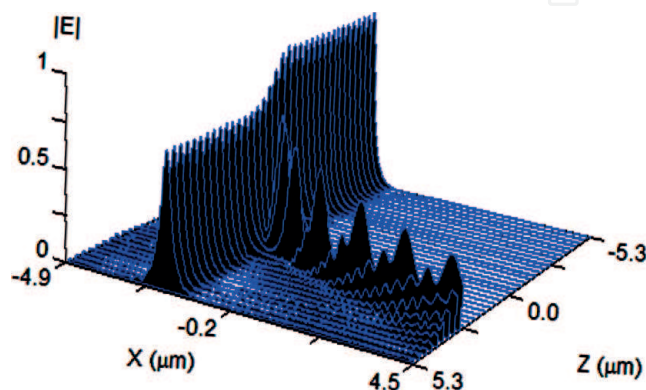


Figure 16.
 CMT method numerical simulation result (from BeamPROP[®] tool) for all-pass FOPRRI configuration (resonance at 1285 nm).

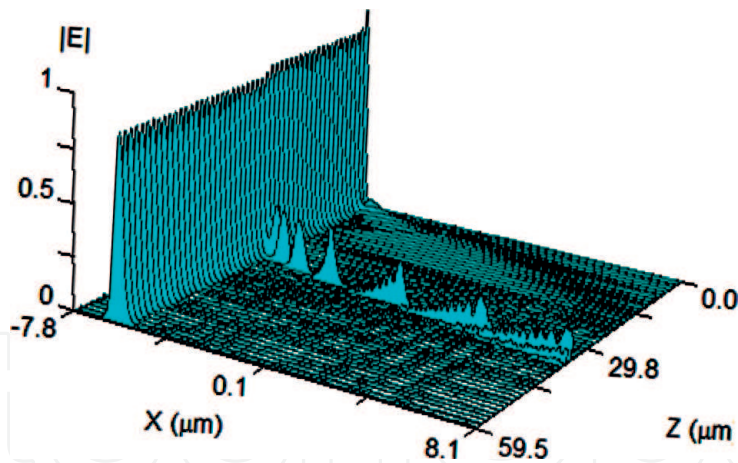


Figure 17.
FEM numerical simulation (from FemSIM[®] tool) for all-pass FOPRRI configuration (resonance at 1285 nm).

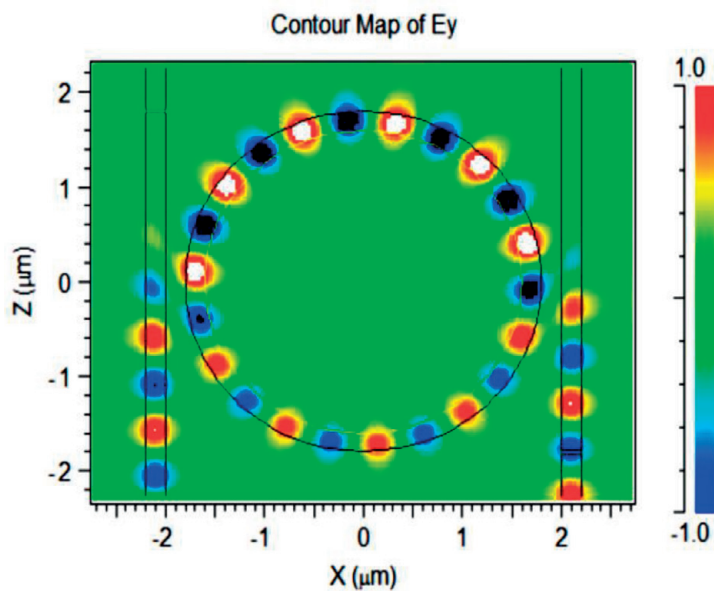


Figure 18.
2D-FTDT numerical simulation results for an add-drop FOPRRI (resonance at 1285 nm).

optical switch, inertial rotation sensor, photonic biosensor, tailored response filter and active ring modulator.

6. Performance comparison of numerical simulation methods used

Table 2 shows performance comparison of all four methods used (EIM, CMT, FEM and FDTD) for both the configurations: all-pass filter and add-drop filter and

Criterion/Method	EIM	CMT (BPM)	FEM	2D-FDTD/3D-FDTD
Computational time (sec) 2D	< 0.05	<0.10	1.7	4.3
Computational time (sec) 3D	68	100	547	1170
Memory (MByte)	16	17	17	17
Error (%)	<7	<1	<1	<1

Table 2.
Comparison of computational time, memory resources and error methods (EIM, CMT, FEM and FDTD).

taking into account three criteria: spent computational time (seconds), memory resources applied (MByte) and error found (%).

7. Conclusions

A conventional model of a fiber optic passive ring resonator interferometer (FOPRRI) was theoretically analyzed in two main configurations: all-pass filter and add-drop filter. Then, four numerical simulation methods (EIM, CMT, FEM and 3D-FDTD) are successively applied on each of these two configurations. In both cases, results showed that EIM method is the most suitable when no very accuracy of results is needed (error < 7%) and low time of computation is desirable (< 70 s). However, when high accuracy is considered the most important issue, 3D-FDTD is the best method (error < 1%) at the expense of a much larger computing time (≈ 1200 sec) than others. CMT (BPM) method provides substantial performance results with computational time similar than that EIM one, but an error < 1%. Finally, FEM is suitable for simulations that can be approximated with 2D techniques since it provides substantial performance results (error < 1%) with computational time only an order of magnitude above EIM or CMT.

Acknowledgements


The author wishes to thank the Integrated Optics and Optoelectronics Laboratory of Faculty of Sciences of University of Oviedo-Spain for technical support and assistance provided in the realization of this work.

Author details

Ramón José Pérez Menéndez
UNED, Lugo, Spain

*Address all correspondence to: ramonjose.perez@lugo.uned.es

IntechOpen

© 2018 The Author(s). Licensee IntechOpen. This chapter is distributed under the terms of the Creative Commons Attribution License (<http://creativecommons.org/licenses/by/3.0>), which permits unrestricted use, distribution, and reproduction in any medium, provided the original work is properly cited. 

References

- [1] Hariharan P. Optical Interferometry. 2nd ed. London: Elsevier, Academic Press; 2003
- [2] Sharma U, Wei X. Fiber optic interferometric devices. Chapter 2. In: Kang JU, editor. Fiber Optic Sensing and Imaging. New York: Springer; 2013. pp. 29-53
- [3] Yin S, Ruffin PB, Yu FTS, editors. Fiber Optic Sensors. 2nd ed. Boca Raton FL (USA): CRC Press; 2008. pp. 333-366
- [4] Yariv A, Yeh P. Optical Resonators from Photonics. Chapter 4. 6th ed. Oxford University Press, New York; 2007. pp. 156-210
- [5] Vali V, Shorthill RW. Fiber ring interferometer. Applied Optics. 1976; **15**(5):1099-2000
- [6] Vali V, Shorthill RW. Fiber laser gyroscopes. Proceedings of SPIE. 1976; **76**:110
- [7] Vali V, Shorthill RW. Ring interferometer 950 m long. Applied Optics. 1977; **16**:290
- [8] Ezequiel S, Balsamo SR. Passive ring resonator laser gyroscope. Applied Physics Letters. 1977; **30**:478
- [9] Meyer RE, Ezequiel S. Passive fiber-optic ring resonator for rotation sensing. Optics Letters. 1984; **8**:644-646
- [10] Rao YJ, Jackson DA. Principles of fiber-optic interferometry. In: Grattan LS, Meggitt BT, editors. Optical Fiber Sensor Technology. Boston, MA: Springer; 2000. pp. 167-191
- [11] Yve CY, Peng JD, Liao YB, Zhou BK. Fibre ring resonator with finesse of 1260. Electronics Letters. 1988; **24**:622-623
- [12] Stokes LF, Chodorow M, Shaw HJ. All-single-mode fiber resonator. Optics Letters. 1982; **7**:288-290
- [13] Stokes LF, Chodorow M, Shaw HJ. All-fiber stimulated Brillouin ring laser with sub-milliwatt pump threshold. Optics Letters. 1982; **7**:509-511
- [14] Jackson DA, Jones JDC. Fiber-optic sensors. Optica Acta. 1986; **33**:1469-1503
- [15] Zarinetchi F, Smith SP, Ezekiel S. Stimulated Brillouin fiber-optic laser gyroscope. Optics Letters. 1991; **16**: 229-231
- [16] Hill KO, Kawasaki BS, Johnson DC. CW Brillouin laser. Applied Physics Letters. 1976; **28**:608-609
- [17] Kalli K, Jackson DA. Ring resonator optical spectrum analyzer with 20 kHz resolution. Optics Letters. 1992; **17**: 1090-1092
- [18] Tai S, Kyuma K, Nakayama T. Novel measuring method for spectral linewidth of laser diodes using fiber-optic ring resonators. Electronics Letters. 1985; **21**:91-93
- [19] Newton SA, Howland RS, Jackson KP, Shaw HJ. High speed pulse-train generation using single-mode fiber recirculating delay lines. Electronics Letters. 1983; **19**:757-758
- [20] Rabus D. Integrated Ring Resonators. New York: Springer; 2007
- [21] Heebner JE et al. Optical Micro-Resonators: Theory, Fabrication and Applications. London: Springer; 2008
- [22] Heebner JE, Wong V, Schweingsberg A, Boyd RW, Jackson DJ. Optical transmission

characteristics of fiber ring resonators. *IEEE Journal of Quantum Electronics*. 2004;**40**:736-730

[23] Vien V. *Optical Micro-Ring Resonators: Theory, Techniques and Applications*. Boca Raton, FL: CRC Press; 2017

[24] Bogaerts W et al. Silicon micro-ring resonators. *Laser and Photonics Reviews*. 2012;**6**(1):47-53

[25] Knox RM, Thoullos PP. Integrated circuits for the millimeter through optical frequency range. In: *Proceedings of Symposium on Submillimeter Waves*. Vol. 20; Brooklyn-New York; 1970. pp. 497-515

[26] Marcatili EA. Dielectric rectangular waveguide and directional coupler for integrated optics. *The Bell System Technical Journal*. 1969;**48**:2071-2102

[27] Mode Solutions-Waveguide Mode Solver and Propagation Simulator. URL: <http://www.lumerical.com/mode>

[28] WGMODES-Photonics Research Laboratory. URL: <http://www.photonics.umd.edu/software/wgmodes/>

[29] COMSOL Multiphysics. URL: <http://comsol.com/mode>

[30] Phoenix Software. URL: <http://www.phoenixbv.com/FieldDesigner>

[31] Yariv A. Coupled-mode theory for guided-wave optics. *IEEE Journal of Quantum Electronics*. September 1973; **QE-9**(9):919-9333

[32] RSoft Products-Synopsys Optical Solutions. URL: <http://optics.synopsys.com/RSoft/BeamPROP>

[33] Phoenix Software. URL: <http://www.phoenixbv.com/OptoDesigner>

[34] RSoft Products-Synopsys Optical Solutions. URL: <http://optics.synopsys.com/RSoft/FemSIM>

[35] FDTD Solutions-Lumerical's Nanophotonic FDTD Simulation Software. URL: <http://lumerical.com/fdtd>

[36] RSoft Products-Synopsys Optical Solutions. URL: <http://optics.synopsys.com/RSoft/FullWAVE>

[37] Feit MD, Freck JA Jr. Light propagation in graded-index optical fibers. *Applied Optics*. 1978;**17**: 3990-3998

[38] Thylén L. The beam propagation method: An analysis of its applicability. *Optics Quantum Electron*. 1983;**15**: 433-439

[39] Yamauchi J, Shibayama J, Nakano H. Beam propagation method using Padé approximant operators. *Transactions IEICE Japan*. 1994;**J-77-C-I**: 490-494

[40] Hadley GR. Wide-angle beam propagation using Padé approximant operators. *Optics Letters*. 1992;**17**: 1426-1428

[41] Liu PL, Li BJ. Study on form birefringence in waveguide devices using the semi-vectorial beam propagation method. *IEEE Photonics Technology Letters*. 1991;**3**: 913-915

[42] Koshiba M, Tsuji Y. A wide-angle finite element beam propagation method. *IEEE Photonics Technology Letters*. 1996;**8**:1208-1210

[43] Zienckiewicz OC. *The Finite Element Method*. 3rd ed. New York: McGraw-Hill; 1973

[44] Koshiha M, Saitoh H, Eguchi M, Hirayama K. Simple scalar finite element approach to optical waveguides. *IEEE Proceedings Journal*. 1992;**139**:166-171

[45] Koshiha M. *Optical Waveguide Theory by the Finite Element Method*. Dordrecht, Holland: KTK Scientific Publishers and Kluwer Academic Publishers; 1992

[46] Meunier G. *The Finite Element Method for Electromagnetic Modeling*. River Street-Hoboken NJ: John Wiley & Sons; 2008

[47] Kwon YW, Bang H. *The Finite Element Method Using Matlab*. CRC Press; 1977

[48] Stern M. Semivectorial polarized finite difference method optical waveguides with arbitrary index profiles. *IEEE Proceedings Journal*. Piscataway NJ (USA); 1988;**135**:56-63

[49] Stern M. Semivectorial polarized H-field solutions for dielectric waveguides with arbitrary index profiles. *IEEE Proceedings Journal*. Piscataway NJ (USA); 1988;**135**:333-338

[50] Kawano K, Kitoh T, Kohtuku M, Takeshita T, Hasumi Y. 3-D semivectorial analysis to calculate facet reflectivities of semiconductor optical waveguides based on the bi-directional method of line BPM (MoL-BPM). *IEEE Photonics Technology Letters*. 1998;**10**: 108-110

[51] Gerdes B, Lunitz B, Benish D, Pregla R. Analysis of slab waveguide discontinuities including radiation and absorption effects. *Electronics Letters*. 1992;**28**:1013-1015

[52] Taflove A. *Computational Electrodynamics: Finite Difference Time Domain Method*. Artech House: Norwood, MA; 1995